STEADY STATE DUST DISTRIBUTIONS IN DISK VORTICES: OBSERVATIONAL PREDICTIONS AND APPLICATIONS TO TRANSITIONAL DISKS

WLADIMIR LYRA[1,2,4,5] AND MIN-KAI LIN[3,5]
[1] Jet Propulsion Laboratory, California Institute of Technology, 4800 Oak Grove Drive, Pasadena, CA 91109, USA; wlyra@caltech.edu
[2] Division of Geological & Planetary Sciences, California Institute of Technology, 1200 East California Boulevard MC 150-21, Pasadena, CA 91125, USA
[3] Canadian Institute for Theoretical Astrophysics, 60 St. George Street, Toronto, Ontario M5S 3H8, Canada; mklin924@cita.utoronto.ca
Received 2013 May 25; accepted 2013 July 11; published 2013 August 29

ABSTRACT

The Atacama Large Millimeter Array has returned images of transitional disks in which large asymmetries are seen in the distribution of millimeter sized dust in the outer disk. The explanation in vogue borrows from the vortex literature and suggests that these asymmetries are the result of dust trapping in giant vortices, excited via Rossby wave instabilities at planetary gap edges. Due to the drag force, dust trapped in vortices will accumulate in the center and diffusion is needed to maintain a steady state over the lifetime of the disk. While previous work derived semi-analytical models of the process, in this paper we provide analytical steady-steady solutions. Exact solutions exist for certain vortex models. The solution is determined by the vortex rotation profile, the gas scale height, the vortex aspect ratio, and the ratio of dust diffusion to gas-dust friction. In principle, all of these quantities can be derived from observations, which would validate the model and also provide constrains on the strength of the turbulence inside the vortex core. Based on our solution, we derive quantities such as the gas-dust contrast, the trapped dust mass, and the dust contrast at the same orbital location. We apply our model to the recently imaged Oph IRS 48 system, finding values within the range of the observational uncertainties.

Key words: methods: analytical – planet–disk interactions – planets and satellites: formation – protoplanetary disks

Online-only material: color figures

1. INTRODUCTION

Transitional disks are a class of circumstellar disks that lack a significant near-infrared (1–$5\,\mu$m) excess, while showing steep slopes in mid-infrared (5–$20\,\mu$m) and far-infrared ($>20\,\mu$m) excesses typical of classical T-Tauri disks (Strom et al. 1989; Skrutskie et al. 1990; Gauvin & Strom 1992; Wolk & Walter 1996; Calvet et al. 2002, 2005; Muzerolle et al. 2006; Sicilia-Aguilar et al. 2006; Currie et al. 2009; Currie & Sicilia-Aguilar 2011). This "opacity hole" implies the absence of optically thick warm dust in the inner disk, with a dust wall generating the mid-IR emission, followed by cold dust in the outer disk. These observations, together with the age of these systems (in the 1–10 Myr range; see, e.g., Currie 2010 for a review), provide strong evidence that these are objects caught in the evolutionary stage between gas-rich primordial and gas-poor debris disks, hence their name.

Explanations for the opacity hole generally fall in four distinct categories. These are, namely, grain growth and dust settling (Brauer et al. 2007; Dominik & Dullemond 2008; Zsom et al. 2011; Birnstiel et al. 2012), photoevaporation (Alexander et al. 2006; Cieza 2008; Pascucci & Sterzik 2009; Owen et al. 2010), dynamical interaction with close stellar or substellar companions (Ireland & Kraus 2008), and planet formation via dust locking (Safronov 1969; Lyttleton 1972; Goldreich & Ward 1973; Youdin & Shu 2002; Johansen et al. 2007) and gap carving (Papaloizou & Lin 1984; Lin & Papaloizou 1986a, 1986b; Bryden et al. 1999; Paardekooper & Mellema 2004; Quillen et al. 2004; Najita et al. 2007; Andrews et al. 2011). Analyses of individual disks (Calvet et al. 2004, 2005; Espaillat et al. 2008)

tend to favor one process over another, and even census studies of statistically significant samples of disks find one process to be dominant (Najita et al. 2007; Cieza 2008). These seemingly conflicting results in fact illustrate the heterogeneity of transitional disks, where a combination of all the suggested processes are needed to explain the rich diversity observed (Cieza 2010; Muzerolle et al. 2010; Merín et al. 2010; Rosotti et al. 2013; Clarke & Owen 2013).

Recently, high angular resolution imaging of the outer regions of transitional disks have become available, showing a myriad of puzzling asymmetries that beg for explanation. These asymmetries come in the shape of spiral arms (Piétu et al. 2005; Corder et al. 2005; Muto et al. 2012; Tang et al. 2012), elliptical dust walls (Isella et al. 2012), and non-axisymmetric dust clouds (Oppenheimer et al. 2008; Brown et al. 2009; Casassus et al. 2012). In particular, giant horseshoe-shaped dust distributions are seen in images obtained with the Combined Array for Research in Millimeter-wave Astronomy (Isella et al. 2013) and with the Atacama Large Millimeter Array (ALMA; Casassus et al. 2013; van der Marel et al. 2013). The planet interpretation is particularly attractive for explaining these asymmetries, since they generally match the range of structures predicted by hydrodynamical models of planet–disk interactions.

A deep gap is one of the expected structures, as the planet tides expel material from the vicinity of its orbit (Papaloizou & Lin 1984; Lin & Papaloizou 1986a, 1986b; Nelson et al. 2000; Masset & Snellgrove 2001; Paardekooper & Mellema 2004; Quillen et al. 2004; de Val-Borro et al. 2006; Klahr & Kley 2006; Lyra et al. 2009a; Zhu et al. 2011; Kley et al. 2012; Kley & Nelson 2012). The gas gap walls constitute steep pressure gradients that, by modifying the rotational profile locally, are prone to excite what has been called the Rossby wave instability (RWI; Lovelace & Hohlfeld 1978; Toomre 1981; Papaloizou &

---

[4] Sagan Fellow.
[5] Both authors contributed equally to this work.

Pringle 1984, 1985; Hawley 1987; Lovelace et al. 1999). The RWI is an "edge mode" instability, akin to the Kelvin–Helmholtz Instability, that converts the extra shear into vorticity. The large-scale vortices that result are well known in the planet formation literature.

Barge & Sommeria (1995), Adams & Watkins (1995), and Tanga et al. (1996) independently proposed, in the context of primordial disks, that vortices could speed up planet formation by trapping solids of centimeter to meter size. The dynamics of this trapping was developed in a detailed work by Chavanis (2000), setting much of the analytical foundations of the field. Godon & Livio (1999, 2000) and Johansen et al. (2004) simulated vortices numerically, finding fast trapping of particles but also quick dissipation due to (Laplacian) viscosity. These studies, however, did not consider the question of how to form disk vortices in first place, a question tackled by Varnière & Tagger (2006). These authors show that a sharp viscosity gradient in the disk leads to a pile-up of matter, that in turn goes unstable to the RWI. Because the magnetorotational instability (MRI; Balbus & Hawley 1991) leads to a significant turbulent viscosity, Varnière & Tagger (2006) suggest that this mechanism could be at work in the transition between the MRI-active and dead zones. The accumulation of dust in these self-sustained RWI vortices was subsequently studied by Inaba & Barge (2006), albeit in the fluid approach that limited the dust size they could use. Planetary gap edges were seen to excite vortices in many simulations in the code-comparison study of de Val-Borro et al. (2006), an effect later explained in terms of the RWI as well (de Val-Borro et al. 2007).

These efforts culminated in a coherent picture of vortex-assisted planet formation in dead zone vortices by Lyra et al. (2008, 2009a) and in gap edge vortices by Lyra et al. (2009b). These works solved the nonlinear compressible hydrodynamics and the aerodynamics of interacting particles, demonstrating the gravitational collapse of the trapped solids, albeit in two dimensions (2D). The RWI was subsequently studied in barotropic three-dimensional (3D) models by Méheut et al. (2010, 2012a, 2012b, 2012c), who found interesting meridional circulation patterns; in self-gravitating disks with applications to planet migration in 2D (Lin & Papaloizou 2011a, 2011b, 2012) and 3D (Lin 2012b), who find weakening and eventual suppression of the RWI with increasing disk mass; in magnetohydrodynamics by Lyra & Mac Low (2012), bringing realism to the dead-zone scenario; and by Lin (2012a, 2013), who generalized the linear RWI to 3D polytropic and non-barotropic disks, respectively.

Part of these results have been applied to the field of transitional disks. The particle size that is preferentially trapped is set by the friction time, τ_f, which is a function of the gas density and the particle radius. A suitable nondimensionalization for the friction time is the Stokes number, $St = \Omega\tau_f$, where Ω is the Keplerian frequency. Dust that is too well coupled to the gas ($St \to 0$) does not suffer friction, and bodies that are too large ($St \to \infty$) have too much inertia to be moved by the gas; the preferential size for trapping is $St = 1$ (see, e.g., Youdin & Goodman 2005; Youdin 2008). While in the dense, fast rotating, inner regions of primordial disks, the preferentially trapped particle size corresponds to meter size. In the thin, slowly rotating, outer regions of transitional disks, the size corresponding to $St = 1$ drops by about three orders of magnitude (Brauer et al. 2007; Pinilla et al. 2012a). The resulting trapping of submillimeter and millimeter size dust may not lead to the critical densities necessary to form planets, but these trappings may well explain the puzzling observed lopsided asymmetries. While the motivation

and particle sizes are different, the relevant physics is scale-free, and thus identical as long as gravity is not involved.

This property was invoked by Regály et al. (2012) to suggest that the submillimeter observations of Brown et al. (2009) could be the result of dust trapping in Rossby vortices. If indeed this process occurs, then, as the drag force drives dust toward the vortex center, diffusion is needed to maintain a steady state over the lifetime of the disk (Klahr & Henning 1997; Chavanis 2000; Ataiee 2013). Birnstiel et al. (2013) presented a semi-analytical model that solves for the azimuthal dust distribution while using fits from numerical simulations (Pinilla et al. 2012b) to constrain the radial morphology. In this work, we present a fully analytical model for the steady-state distribution of dust trapped in vortices, accurate to first order in Stokes number, and general in space. In Section 2, we derive the advective-diffusive equation and in Section 3 we derive the appropriate coordinate transformation. In Section 4, we solve the equation for the "axisymmetric" case in that coordinate system and in Section 5 we generalize it for non-axisymmetry. In Section 6, we derive observational predictions and apply the model to the Oph IRS 48 system.

2. DUST STEADY STATE

Considering the dust particles are small sizes, we can treat dust as a fluid. The dust should then follow the continuity equation:

$$\frac{\partial \rho_d}{\partial t} = -(\boldsymbol{w} \cdot \boldsymbol{\nabla})\rho_d - \rho_d \boldsymbol{\nabla} \cdot \boldsymbol{w} - \boldsymbol{\nabla} \cdot J, \qquad (1)$$

where ρ_d is the dust density, $\boldsymbol{w}$ is the dust velocity, and J is the diffusion flux. We take the diffusion flux to be:

$$J = -D\,\rho_g \boldsymbol{\nabla}(\rho_d/\rho_g), \qquad (2)$$

as in the contaminant equation (Morfill & Völk 1984; Clarke & Pringle 1988; Charnoz et al 2011), where D is the diffusion coefficient (the diffusion is due to elliptical turbulence in the vortex core and in general will be different from the turbulent viscosity in the disk) and ρ_g is the gas density. We assume that D is constant. A list of the mathematical symbols used in this work, together with their definitions, is provided in Table 1.

To derive the velocities, instead of solving the momentum equations for the dust, we make use of the relative velocity, following Youdin & Goodman (2005, see also Youdin 2008):

$$\boldsymbol{w} = \boldsymbol{u} + \tau_f \boldsymbol{\nabla} h, \qquad (3)$$

where $\boldsymbol{u}$ is the gas velocity. Equation (3) is accurate to first order in friction time τ_f, assumed to be constant. For isentropic gas, the enthalpy h is defined as $dh = dp/\rho_g$, where p is the pressure. As noted by Charnoz et al (2011), Equation (1) can be written as a typical continuity equation with Laplacian diffusion:

$$\partial_t \rho_d = -(\boldsymbol{v} \cdot \boldsymbol{\nabla})\rho_d - \rho_d \boldsymbol{\nabla} \cdot \boldsymbol{v} + D\nabla^2 \rho_d, \qquad (4)$$

provided that the effective velocity $\boldsymbol{v}$ is

$$\boldsymbol{v} \equiv \boldsymbol{w} + D\boldsymbol{\nabla} \ln \rho_g. \qquad (5)$$

For isothermal gas, the extra term is $D/c_s^2 \boldsymbol{\nabla} h$, and, comparing with Equation (3), its effect amounts to redefining the friction time as

$$\tau \equiv \tau_f + \frac{D}{c_s^2}. \qquad (6)$$

Table 1
Symbols Used in This Work

Symbol	Definition	Description
τ_f		Friction time
D		Dust diffusion coefficient
c_s		Sound speed
τ	$= \tau_f + D/c_s^2$	Effective friction time
Ω		Keplerian angular frequency
St	$= \Omega \tau_f$	Stokes number
t		Time
ρ_g, ρ_d		Gas and dust density
$\boldsymbol{u}, \boldsymbol{w}$		Gas and dust velocity
$\boldsymbol{v}$	$= \boldsymbol{w} + D\boldsymbol{\nabla} \ln \rho$	Effective dust velocity
p		Gas pressure
h	$dh = dp/\rho_g$	Gas enthalpy
χ		Vortex aspect ratio (>1)
a		Vortex semi-minor axis
Ω_V		Vortex angular frequency
ω_V	$= \Omega_V/\Omega$	Dimensionless vortex frequency
C	$= -\boldsymbol{\nabla} \cdot \boldsymbol{v}$	
A	$= \Omega_V/D$	
B	$= C/D$	
ν		Azimuth in vortex reference frame
$\xi_\pm$	$= 1 \pm \chi^{-2}$	
H	c_s/Ω	Sonic scale, gas scale height
δ	$D = \delta c_s H$	Dimensionless diffusion parameter
$f(\chi)$	Equation (35)	Scale function
S	$= \text{St}/\delta$	Dimensionless number
H_g	$= H/f(\chi)$	Gas vortex scale length
H_V	$= H_g \sqrt{\frac{1}{S+1}}$	Dusty vortex scale length
k	$= \sqrt{2}/H_V$	
ζ	$= ka$	
$\tilde{\chi}$	$= \frac{\chi^2 - 1}{2(\chi^2 + 1)}$	
β	$= (B_1 - B_2)/4B$	
k_m	$= 1 + imA/B$	
$\mathcal{A}_m \, \mathcal{B}_m \, \mathcal{C}_m$	Equations (40)–(42)	Differential operators
b_m		Constants
$\epsilon(\zeta)$		Non-axisymmetric correction
ε	$= \int \rho_d dV / \int \rho_g dV$	Global dust-to-gas ratio
ρ_0		Max gas density, reference density

Combining Equations (3), (5), and (6), we can thus write

$$\boldsymbol{v} = \boldsymbol{u} + \tau \boldsymbol{\nabla} h, \qquad (7)$$

valid for isothermal gas only.

Inside the vortex, the gas flow is divergent-free, and we adopt the following model for $\boldsymbol{u}$:

$$u_x = \Omega_V y / \chi \qquad u_y = -\Omega_V x \chi, \qquad (8)$$

where $\chi > 1$ is the vortex aspect ratio (it has semi-minor axis a and semimajor axis $a\chi$). Notice that the flow eventually is supersonic for large values of x and y. This result will limit the validity of the solution, as the vortices shock beyond the sonic perimeter. This process effectively leads to a vortex "boundary," beyond which the motion rejoins the background Keplerian flow.

In this work, we consider the Kida solution (Kida 1981):

$$\Omega_V = \frac{3\Omega}{2(\chi - 1)}, \qquad (9)$$

which smoothly matches the above velocity field to the Keplerian shear. We also consider the Goodman–Narayan–Goldreich (GNG) solution (Goodman et al. 1987) that exactly solves the compressible Euler equations:

$$\Omega_V = \Omega \sqrt{3/(\chi^2 - 1)}. \qquad (10)$$

We comment that these solutions make use of the shearing box equations, and are thus subject to the same limitations as that approximation (Regev & Umurhan 2008). In particular, the shearing box does not have a radial vorticity gradient, and thus cannot excite the RWI (Tagger 2001). Nevertheless, independent of the excitation mechanism, these solutions are good local descriptions of the perturbed flow. The GNG solution was used to model vortices found in non-linear hydrodynamic global simulations of the Papaloizou–Pringle instability (Hawley 1987), which is similar to the RWI. Recently, Lin & Papaloizou (2011a) found that, in quasi-steady state, the RWI vortices excited at planetary gap edges resemble vortices formed by perturbing the disk with the Kida solution. We are thus confident that the above solutions are suitable as a first model for disk vortices. Moreover, it is straightforward to generalize the solutions below to any flow in the form $u_x \propto y$ and $u_y \propto -x$.

We note that the dust velocity (Equation (7)) is comprised of a divergent-free part, $\boldsymbol{u}$, and a curl-free part, $\tau \boldsymbol{\nabla} h$. The vortex flow attempts to keep the dust particles on closed elliptic streamlines via $\boldsymbol{u}$, while friction attempts to concentrate dust toward the pressure maximum via $\tau \boldsymbol{\nabla} h$. The only effect that attempts to spread out the dust is diffusion, via D.

Taking the divergence of Equation (7) gives

$$\boldsymbol{\nabla} \cdot \boldsymbol{v} = \tau \nabla^2 h, \qquad (11)$$

and we can find the Laplacian of the enthalpy via the Euler equation. Adopting the shearing sheet approximation, in steady state the force balance yields

$$\frac{\partial h}{\partial x} = 3\Omega^2 x + 2\Omega u_y - u_y \frac{\partial u_x}{\partial y}$$
$$= \left(3\Omega^2 - 2\Omega\Omega_V \chi + \Omega_V^2\right) x = -\frac{C_1}{\tau} x, \qquad (12)$$

$$\frac{\partial h}{\partial y} = -2\Omega u_x - u_x \frac{\partial u_y}{\partial x}$$
$$= \left(-2\Omega\Omega_V/\chi + \Omega_V^2\right) y = -\frac{C_2}{\tau} y. \qquad (13)$$

Substituting the above equations into Equation (11), also with $\omega_v = \Omega_V/\Omega$, the divergence becomes

$$\boldsymbol{\nabla} \cdot \boldsymbol{v} = -(C_1 + C_2) = -C \qquad (14)$$

$$= -\tau\Omega^2 \left[2\omega_v \left(\frac{\chi^2 + 1}{\chi}\right) - \left(2\omega_v^2 + 3\right)\right], \qquad (15)$$

where we define C as positive, so that the divergence is negative (physically meaning that the dust gets trapped). Replacing Equation (14) in the modified continuity equation (Equation (4)), and setting $\partial_t = 0$ for steady state,

$$(D\nabla^2 - \boldsymbol{v} \cdot \boldsymbol{\nabla} + C)\rho_d = 0. \qquad (16)$$

Substituting the gas velocity (Equation (8)), and dividing by D, we arrive at the modified advection-diffusion equation that should determine the steady-state distribution of the vortex-trapped dust,

$$[\nabla^2 - (Ay\chi^{-1} - B_1 x)\partial_x + (Ax\chi + B_2 y)\partial_y + B]\rho_d = 0, \qquad (17)$$

where we also substituted $A = \Omega_V/D$ and $B_i = C_i/D$.

3. CHANGE OF VARIABLE

We change variables to the coordinate system used in Chang & Oishi (2010):

$$x = a \cos v, \qquad (18)$$

$$y = a \chi \sin v. \qquad (19)$$

The system is not orthogonal, but it has the advantage of matching the aspect ratio of the ellipses. (In contrast, the elliptical coordinate system, although orthogonal, describes a system of confocal ellipses of different aspect ratios that does not coincide with the geometry of the problem.) In these coordinates, the transformations are

$$\begin{bmatrix} \partial_a \\ \partial_v \end{bmatrix} = \mathbf{A} \begin{bmatrix} \partial_x \\ \partial_y \end{bmatrix} \quad \text{and} \quad \begin{bmatrix} \partial_x \\ \partial_y \end{bmatrix} = \mathbf{A}^{-1} \begin{bmatrix} \partial_a \\ \partial_v \end{bmatrix}, \qquad (20)$$

with

$$\mathbf{A} = \begin{bmatrix} \frac{\partial x}{\partial a} & \frac{\partial y}{\partial a} \\ \frac{\partial x}{\partial v} & \frac{\partial y}{\partial v} \end{bmatrix} = \begin{bmatrix} \cos v & \chi \sin v \\ -a \sin v & a \chi \cos v \end{bmatrix}. \qquad (21)$$

The inverse matrix is

$$\mathbf{A}^{-1} = \frac{1}{a\chi} \begin{bmatrix} a\chi \cos v & -\chi \sin v \\ a \sin v & \cos v \end{bmatrix}. \qquad (22)$$

The transformations are therefore

$$\frac{\partial}{\partial x} = \cos v \frac{\partial}{\partial a} - \frac{\sin v}{a} \frac{\partial}{\partial v}, \qquad (23)$$

$$\frac{\partial}{\partial y} = \frac{1}{\chi} \left(\sin v \frac{\partial}{\partial a} + \frac{\cos v}{a} \frac{\partial}{\partial v} \right), \qquad (24)$$

and the Laplacian is thus

$$\nabla^2 = \frac{1}{2} [\xi_- \cos 2v + \xi_+] \partial_a^2$$
$$+ \frac{1}{2a^2} [\xi_+ - \xi_- \cos 2v] \partial_v^2$$
$$- \frac{\sin 2v}{a} \xi_- \partial_{av}^2$$
$$+ \frac{1}{2a} [\xi_+ - \xi_- \cos 2v] \partial_a$$
$$+ \frac{\sin 2v}{a^2} \xi_- \partial_v, \qquad (25)$$

with $\xi_\pm = (1 \pm \chi^{-2})$. As for the advection term, we have

$$\boldsymbol{v} \cdot \boldsymbol{\nabla} = (\boldsymbol{u} + \tau \boldsymbol{\nabla} h) \cdot \boldsymbol{\nabla}$$
$$= - \left[\Omega_V - \frac{\sin 2v}{2}(C_1 - C_2) \right] \partial_v$$
$$- (C_1 \cos^2 v + C_2 \sin^2 v) a \, \partial_a. \qquad (26)$$

The dust-trapping equation is therefore

$$\left\{ \nabla^2 + \left[A - \frac{\sin 2v}{2}(B_1 - B_2) \right] \partial_v \right.$$
$$+ \left. (B_1 \cos^2 v + B_2 \sin^2 v) a \, \partial_a + B \right\} \rho_d = 0. \qquad (27)$$

4. "AXISYMMETRIC" SOLUTION

4.1. Dust Distribution

We now make the assumption that the dust distribution follows, in shape, that of the gas (we will relax this approximation in the next section). In this case, the dust distribution follows ellipses of equal aspect ratios. So, $\partial_v = 0$, "axisymmetric" in (a, v) coordinates. Equation (27) then becomes:

$$\left\{ \frac{1}{2} (\xi_- \cos 2v + \xi_+) \partial_a^2 + \left[\frac{1}{2a} (\xi_+ - \xi_- \cos 2v) \right. \right.$$
$$+ \left. \left. (B_1 \cos^2 v + B_2 \sin^2 v) a \right] \partial_a + B \right\} \rho_d = 0. \qquad (28)$$

We now integrate the above equation in v, from 0 to 2π. This step yields

$$\left[\partial_a^2 + \left(\frac{1}{a} + \frac{k^2}{2} a \right) \partial_a + k^2 \right] \rho_d = 0, \qquad (29)$$

where we define $k^2 = 2B/\xi_+$. Note that the parameter A is absent because it represents advection by the vortex, which only moves dust particles along the same ellipse, not across it. It is not relevant in the v-averaged problem. The solution of Equation (29) is

$$\rho_d(a) = \exp\left(-\frac{k^2 a^2}{4} \right) \left[c_1 + c_2 \mathrm{Ei}\left(\frac{k^2 a^2}{4} \right) \right], \qquad (30)$$

where c_1 and c_2 are constants and $\mathrm{Ei}(x)$ is the exponential integral function. Since it diverges at the origin, c_2 has to be zero, and

$$\rho_d(a) = \rho_{d\,\mathrm{max}} \, \exp\left(-\frac{a^2}{2H_V^2} \right), \qquad (31)$$

with $H_V = \sqrt{2}/k$ for symmetry with the gas sonic scale. We can rewrite this length scale recalling that $k^2 = 2B/\xi_+$ and $B = C/D$. We can substitute the diffusion coefficient $D = \delta \Omega H^2$, where δ is a dimensionless coefficient, and $\mathrm{St} = \tau_f \Omega$ for the Stokes number, thus writing:

$$k^2 = \frac{2(\mathrm{St} + \delta)}{\delta H^2} f^2(\chi), \qquad (32)$$

so

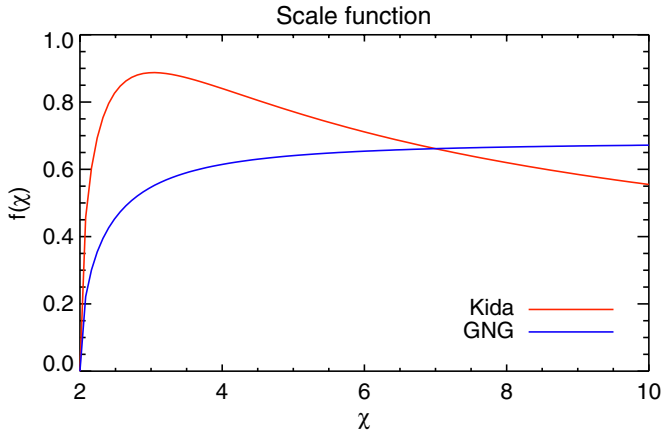$$H_V = \frac{H}{f(\chi)} \sqrt{\frac{\delta}{\mathrm{St} + \delta}}. \qquad (33)$$

Following Jacquet et al. (2012), we define $S = \mathrm{St}/\delta$. The vortex scale length is therefore:

$$H_V = \frac{H}{f(\chi)} \sqrt{\frac{1}{S + 1}}. \qquad (34)$$

In these equations, the scale function $f(\chi)$ is given by

$$f^2(\chi) = \xi_+^{-1} \left[2\omega_v \left(\frac{\chi^2 + 1}{\chi} \right) - (2\omega_v^2 + 3) \right]$$
$$= 2\omega_v \chi - \xi_+^{-1}(2\omega_v^2 + 3), \qquad (35)$$

and depends on the vortex solution used. We plot $f(\chi)$ for the Kida and GNG solutions in Figure 1. These solutions are defined in the real axis only for $\chi > 2$ ($f^2 < 0$ for $0 < \chi < 2$).

Figure 1. Scale function $f(\chi)$, defined by Equation (35), for the Kida ($\Omega_V = 3/2\,\Omega_K/(\chi - 1)$) and the GNG ($\Omega_V = \Omega_K\sqrt{3/(\chi^2 - 1)}$) solutions, respectively. The scale function is related to the square root of the negative of the divergence (Equation (15)), and defined only for $\chi > 2$. For smaller χ, the divergence flips positive, meaning that dust is expelled from the vortex instead of getting trapped. This result happens because of the correlation between Ω_V and χ. The aspect ratio shrinks as the vortex intensifies. At some point, the vortex rotates too fast, and particles are expelled by centrifugal force.

(A color version of this figure is available in the online journal.)

The Goodman solution tends to an asymptote around 0.7. The Kida solution has a tail around 0.5 ± 0.25 in the interval of physical relevance ($2 < \chi \lesssim 10$).

We show in Figure 2, in the inertial frame, the dust distribution for $S = 1$ in a Kida vortex of $\chi = 4$ embedded in a disk of aspect ratio $H/r = 0.1$, where r is the stellocentric distance. We caution that this image extrapolates the spatial range of applicability of the shearing box approximation used to construct the solution.

It is worth noting that for certain vortex models and/or aspect ratios, the Gaussian solution, Equation (31), is in fact an exact solution to the dust-steady-state equation, Equation (27). We will explore this finding in more detail in Section 5, but one can check this fact by inserting Equation (31) into Equation (27) and finding the condition such that the coefficient of the trigonometric terms vanishes. In this special case, explicitly averaging over ν is not required to remove the ν dependence from the problem.

4.2. Gas Distribution

Equation (31) allows us to calculate the gas distribution. We recall that for tracer particles (St $= 0$), the dust distribution should mimic that of the gas. The distribution should thus be

$$\rho_g(a) = \rho_{g\,\mathrm{max}}\,\exp\left(-\frac{a^2}{2H_g^2}\right), \qquad (36)$$

with

$$H_g = H_V|_{\mathrm{St}=0} = H/f(\chi) \qquad (37)$$

and $\rho_{g\,\mathrm{max}}$, the maximum gas density.[6]

Note that for St $= 0$, the effect of diffusion cancels out. This result is because the diffusion is proportional to the gradient of the dust-to-gas ratio (Equation (2)), which is zero for tracer particles.

---

[6] Note that Equation (36) is the gas density averaged over ν at a fixed a. One may directly integrate the gas momenta equations to see that the gas density/pressure depends, in general, on both a and ν.
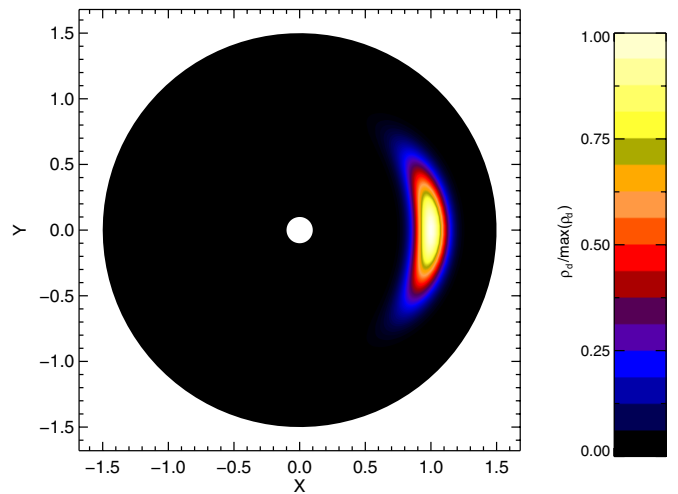
Figure 2. Three parameters, plus a vortex solution, control the dust distribution. The figure shows the appearance of the dust trapped in a Kida vortex of $\chi = 4$, for $S = 1$, in a disk of aspect ratio $H/r = 0.1$.

(A color version of this figure is available in the online journal.)

5. NON-AXISYMMETRIC CORRECTIONS

We now consider the non-axisymmetric problem ($\partial_\nu \neq 0$). We explicitly show that such effects are small in the vortex core provided the effective Stokes number $\overline{\mathrm{St}} \equiv \mathrm{St} + \delta$ is not large. These requirements will become apparent as we proceed through the solution method. In this section, we consistently refer to "axisymmetric" as ν-symmetry in the coordinate system defined by Equations (18) and (19).

5.1. Conversion to Ordinary Differential Equations

The dust density ρ_d is periodic in the ν coordinate. We therefore seek solutions of the form:

$$\rho_d(a, \nu) = \mathrm{Re}\left[\sum_{n=0}^{\infty} \rho_n(a)\exp(\mathrm{i}n\nu)\right]. \qquad (38)$$

For convenience, we will hereafter drop the real part notation. Inserting Equation (38) into the partial differential equation (Equation (27)), multiplying by $\exp(-\mathrm{i}m\nu)$, and integrating the resulting expressions over the ν coordinate, we arrive at a set of coupled ordinary differential equations (ODEs):

$$\mathcal{B}_m\rho_{m-2}(\zeta) + \mathcal{A}_m\rho_m(\zeta) + \mathcal{C}_m\rho_{m+2}(\zeta) = 0, \qquad (39)$$

where $\zeta \equiv ka$, and

$$\mathcal{B}_m \equiv \tilde{\chi}\frac{d^2}{d\zeta^2} + \left[\beta\zeta - \frac{2\tilde{\chi}}{\zeta}\left(m - \frac{3}{2}\right)\right]\frac{d}{d\zeta} + (m-2)\left(\frac{m\tilde{\chi}}{\zeta^2} - \beta\right), \qquad (40)$$

$$\mathcal{A}_m \equiv \frac{d^2}{d\zeta^2} + \left(\frac{1}{\zeta} + \frac{\zeta}{2}\right)\frac{d}{d\zeta} + \left(k_m^2 - \frac{m^2}{\zeta^2}\right), \qquad (41)$$

$$\mathcal{C}_m \equiv \tilde{\chi}\frac{d^2}{d\zeta^2} + \left[\beta\zeta + \frac{2\tilde{\chi}}{\zeta}\left(m + \frac{3}{2}\right)\right]\frac{d}{d\zeta} + (m+2)\left(\frac{m\tilde{\chi}}{\zeta^2} + \beta\right), \qquad (42)$$

where $\tilde{\chi} \equiv (\chi^2 - 1)/[2(\chi^2 + 1)]$, $k_m^2 \equiv 1 + \mathrm{i}mA/B$, and

$$\beta \equiv \frac{B_1 - B_2}{2k^2(1 + \chi^{-2})} = \frac{B_1 - B_2}{4B}. \qquad (43)$$

Note that β is a function of the aspect ratio depending on the vortex model. Equation (39) holds for all m except for $m = 0$, for which the ρ_{m-2} terms are absent. Each ρ_m couples to $\rho_{m\pm2}$ through the operators $\mathcal{B}_m$ and $\mathcal{C}_m$. The axisymmetric problem is recovered by setting $\rho_{m>0} = 0$.

We expect $\rho_d(a, \nu)$ to have even symmetry in ν because of the elliptical nature of the vortex streamlines. Henceforth, we only consider even m values. We seek solutions with $\rho'_m(0) = 0$ (where the prime denotes derivative with respect to the argument) and $\rho_{m\geqslant2}(0) = 0$, so that $\partial_x\rho_d = \partial_y\rho_d = 0$ at the origin, consistent with dust reaching maximal density there.

5.2. Operator Properties

Consider

$$g_m(\zeta) \equiv \zeta^m \exp\left(-\zeta^2/4\right). \tag{44}$$

Then, we find that

$$\mathcal{B}_m g_{m-2} = \frac{1}{4}(\tilde{\chi} - 2\beta)\, g_m, \tag{45}$$

$$\mathcal{A}_m g_m = \left(k_m^2 - \frac{m}{2} - 1\right) g_m, \tag{46}$$

$$\mathcal{C}_m g_{m+2} = \left[4\tilde{\chi}(m+1)(m+2) + 2(\beta - \tilde{\chi})(m+2)\zeta^2 \right. \\ \left. + \frac{(\tilde{\chi} - 2\beta)}{4}\zeta^4\right] g_m. \tag{47}$$

The first two expressions will be useful for constructing nearly axisymmetric solutions.

5.3. Exact Axisymmetric Solutions

It is useful to see how the above formulation connects with the axisymmetric solutions discussed in the previous section. Consider the special case where $\tilde{\chi} = 2\beta$, so that $\mathcal{B}_m g_{m-2} = 0$. Then, the complete solution to Equation (39) is $\rho_0 = b_0 e^{-\zeta^2/4}$ with $\rho_{m>0} \equiv 0$, and b_0 is an arbitrary constant. That is, if $\tilde{\chi} = 2\beta$, then the dust distribution is exactly axisymmetric.

5.3.1. Dust in a GNG Vortex is Axisymmetric

For the GNG vortex, one can verify that $\tilde{\chi} \equiv 2\beta$, implying that the dust density only depends on the ellipse under consideration, not the position along it. This result is true because the GNG vortex has no pressure gradient along the elliptical streamlines (Chang & Oishi 2010).

5.3.2. Condition for Dust in a Kida Vortex to be Axisymmetric

For the Keplerian Kida vortex, we find

$$\tilde{\chi} - 2\beta = \frac{\chi(\chi-1)(\chi-7)}{2(\chi-2)(2\chi+1)(\chi^2+1)}. \tag{48}$$

The dust distribution is exactly axisymmetric for aspect ratio $\chi = 7$, which is also when the Keplerian Kida vortex has no pressure gradient along its elliptical streamlines (Chang & Oishi 2010).

5.4. Source Term Approximation

In preparation for constructing non-axisymmetric solutions, we here describe the *source term approximation* (Zhang & Lai 2006). We assume that $|\rho_m|$ decreases with m, so that in Equation (39) the $\mathcal{C}_m\rho_{m+2}$ term has the smallest magnitude. Neglecting this term as a first approximation, we solve

$$\mathcal{A}_m\rho_m = \begin{cases} 0 & m = 0 \\ -\mathcal{B}_m\rho_{m-2} & m \geqslant 2. \end{cases} \tag{49}$$

The solutions are

$$\rho_m(\zeta) = b_m g_m(\zeta), \tag{50}$$

with

$$b_m = -\frac{(\tilde{\chi} - 2\beta)}{2\left[2k_m^2 - (m+2)\right]} b_{m-2} \tag{51}$$

for $m \geqslant 2$, and b_0 is arbitrary as before. Note that $b_m = 0$ for odd m because $b_1 = 0$ since we require $\rho'_1(0) = 0$. Then, by induction

$$b_m = (-1)^{m/2}\frac{(\tilde{\chi}/2 - \beta)^{m/2}}{\prod_{l=1}^{m/2}\left(2k_{2l}^2 - 2l - 2\right)}b_0, \tag{52}$$

for even $m \geqslant 2$.

The source term approximation assumes $R \equiv |\mathcal{C}_m\rho_{m+2}|/|\mathcal{A}_m\rho_m| \ll 1$. For given ζ, the solution $\rho_m = b_m g_m$ is consistent with this requirement if $|k_m^2| \gg 1$, corresponding to a small effective Stokes number. However, this approximation will eventually fail for large ζ because the solution above implies $R \propto \zeta^4$ for $\zeta \gg 1$. Thus, the solution is only self-consistent for sufficiently small ζ and/or $\overline{\text{St}}$. Nevertheless, we comment that the closed-formed solutions obtained here may be useful in an iterative scheme to obtain numerical solutions to the full set of ODEs.

5.5. Weakly Non-axisymmetric Dust Distributions

We are now ready to construct non-axisymmetric solutions. Consider a Keplerian Kida vortex with $\chi \neq 7$, meaning that the effective frictional force on the dust has a non-vanishing component along the fluid velocity vector (i.e., dust particles are accelerated along the ellipse). We assume that non-axisymmetry in the dust distribution is sufficiently weak, so one may truncate the series solution at $m = 2$. Thus, we set $\rho_{m>2} \equiv 0$. Let

$$\rho_0(\zeta) = b_0 g_0(\zeta) + \epsilon(\zeta), \tag{53}$$

where $\epsilon(x)$ represents the correction to the axisymmetric solution due to $\rho_2(\zeta)$. The ODEs to be solved are

$$\mathcal{A}_0\epsilon(\zeta) = -\mathcal{C}_0\rho_2(\zeta), \tag{54}$$

$$\mathcal{A}_2\rho_2(\zeta) = -\mathcal{B}_2\left(b_0 g_0 + \epsilon\right). \tag{55}$$

To make further progress, we assume at this stage that the ϵ term in Equation (55) can be neglected, so $\rho_2 = b_2 g_2$ with b_2 given by the source term approximation. This methodology means that

$$\frac{\rho_2}{\rho_0} = \frac{b_2}{b_0}\zeta^2, \tag{56}$$

implying that non-axisymmetry becomes significant for sufficiently large ζ, and truncating the series at $m = 2$ is no longer

self-consistent. However, in practice, the ratio $|b_2/b_0|$ is small. For example, inserting $\chi = 4$ gives $|b_2/b_0| \simeq 0.1\%$ for $\overline{\mathrm{St}} = 0.1$ and $|b_2/b_0| \sim 1\%$ for $\overline{\mathrm{St}} = 1$. Since most of the dust is contained within $\zeta \lesssim 1$, we conclude that non-axisymmetry is in general a small effect.

We can use Equation (56) in Equation (54) to calculate the correction term ϵ. We find

$$\epsilon(\zeta) = \frac{1}{8}b_2 g_2[-16\tilde{\chi} + (\tilde{\chi} - 2\beta)\zeta^2]. \tag{57}$$

Collecting the above results and Taylor expanding the g_ms, our weakly non-axisymmetric solution for $\zeta \ll 1$ gives

$$\rho_0(\zeta) = 1 - \frac{\zeta^2}{4}\left[1 - \frac{\tilde{\chi}(\tilde{\chi} - 2\beta)}{iA/B - 1/2}\right] + O(\zeta^4), \tag{58}$$

$$\rho_2(\zeta) = -\frac{(\tilde{\chi} - 2\beta)}{2(4iA/B - 2)}\zeta^2 + O(\zeta^4), \tag{59}$$

where we have used the definition of k_m and set $b_0 = 1$ without loss of generality. In the previous section, we obtained the axisymmetric solution assuming that the non-axisymmetric components were negligible. Here, we see explicitly that the axisymmetric solution in fact leads to non-axisymmetry through the coupling terms, but that these corrections are small for $\overline{\mathrm{St}} \ll 1$, because $B \propto \overline{\mathrm{St}}$. We conclude that dust in the vortex core is effectively axisymmetric.

5.5.1. Consistency Check

Using the above expression for $\epsilon(\zeta)$, we can evaluate $\mathcal{B}_2\epsilon(\zeta)$ in order to assess our assumption that $\epsilon(\zeta)$ makes a negligible contribution to ρ_2. We find

$$\mathcal{B}_2\epsilon(\zeta) = [32\tilde{\chi}(5\tilde{\chi} - 6\beta) - 16(\tilde{\chi} - 2\beta)(2\tilde{\chi} - \beta)\zeta^2$$
$$+ (\tilde{\chi} - 2\beta)^2\zeta^4]\frac{b_2 g_2}{32}. \tag{60}$$

Provided that $|k_2^2| \gg 1$ and ζ is not large, this term is indeed small compared to the first term on the right-hand side of Equation (55). For example, considering $\zeta = 1$, for $\chi = 4$ and $\overline{\mathrm{St}} = 0.1$, we obtain $|\mathcal{B}_2\epsilon|/|\mathcal{B}_2\rho_0| \simeq 0.02$. Even with $\overline{\mathrm{St}} = 1$, this ratio ~ 0.2 is not large. We conclude that our solution procedure above is self-consistent.

6. OBSERVATIONAL PREDICTIONS

Having arrived at the "axisymmetric" solutions (in the a–v plane; Section 4), and shown that deviations from v-symmetry are small (Section 5), we go back to the solutions of Section 4 to derive observational predictions.

6.1. Dust–Gas Contrast

Equations (31) and (36) also allow us to calculate the gas–dust-density contrast, and, therefore, $\rho_{d\,\mathrm{max}}$ as a function of $\rho_{g\,\mathrm{max}}$. For that, we calculate the volume integrals of ρ_d and ρ_g. These, in turn, need the dependencies on the vertical coordinates z. These are straightforward, being $\exp(-z^2/2H^2)$ for the gas and $\exp(-z^2/2H_d^2)$ for the dust, with $H_d = H/\sqrt{(1+S)}$ (Dubrulle et al. 1995). Integrated over plus and minus infinity,
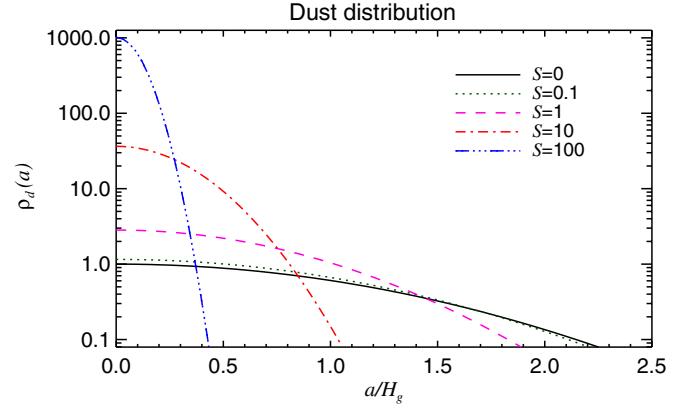
Figure 3. Dust distribution for the "axisymmetric" case (in the coordinate system defined by Equations (18) and (19)). The maximum density is proportional to $(S + 1)^{3/2}$. Curves for $S = 0$, 0.1, 1, 10, and 100 are shown. The $S = 0$ case represents tracer particles and, consequently, the gas density. The x-axis is a/H_g, where $H_g = H/f(\chi)$ is the vortex scale length in the gas phase; H is the sonic scale and $f(\chi)$ is the model-dependent scale function (Equation (35)).
(A color version of this figure is available in the online journal.)

these terms yield $\sqrt{2\pi}\,H$ and $\sqrt{2\pi}\,H_d$, respectively. We thus have

$$\int \rho_d(a, z)dV = \rho_{d\,\mathrm{max}}\frac{(2\pi)^{3/2}}{\sqrt{S+1}}H\int_0^\infty e^{-a^2/2H_g^2\,(S+1)}\,a\chi\,da$$
$$= \rho_{d\,\mathrm{max}}\left(\frac{2\pi}{S+1}\right)^{3/2}\chi HH_g^2, \tag{61}$$

$$\int \rho_g(a, z)dV = \rho_{g\,\mathrm{max}}(2\pi)^{3/2}H\int_0^\infty e^{-a^2/2H_g^2}\,a\chi\,da$$
$$= \rho_{g\,\mathrm{max}}(2\pi)^{3/2}\chi HH_g^2. \tag{62}$$

Dividing Equation (61) by Equation (62), the ratio of the integrals on the left-hand side is the global dust-to-gas ratio, ε. The density enhancement factor is thus

$$\rho_{d\,\mathrm{max}} = \varepsilon\,\rho_0\,(S+1)^{3/2}, \tag{63}$$

where $\rho_0 = \rho_{g\,\mathrm{max}}$ is an appropriate reference density. The full expression for the dust density is therefore

$$\rho_d(a, z) = \varepsilon\,\rho_0\,(S+1)^{3/2}\,\exp\left\{-\frac{[a^2 f^2(\chi) + z^2]}{2H^2}(S+1)\right\}. \tag{64}$$

Equation (63) shows that the dust-to-gas ratio at the origin (vortex center) is related to the total dust-to-gas mass ratio by a simple function of S. In this enhancement, only a third (in log) is caused by sedimentation. The rest is due to in-plane vortex capturing. Midplane dust distributions for different values of S are plotted in Figure 3 as a function of a/H_g.

6.2. Trapped Mass

For the total trapped mass, we simply need to integrate Equation (64), which amounts to replacing Equation (63) in Equation (61):

$$\int \rho_d(a, z)dV = (2\pi)^{3/2}\,\varepsilon\,\rho_0\,\chi HH_g^2 \tag{65}$$

6.3. Dust-density Contrast

The contrast in the same orbit is found by calculating the minimum dust density and comparing it to Equation (63). By substituting the gas solution (Equation (36)) into Equation (31), we can write

$$\frac{\rho_{d\,\max}}{\rho_{d\,\min}} = \frac{\rho_{g\,\max}}{\rho_{g\,\min}} \exp(S), \qquad (66)$$

which is the same result as found by Birnstiel et al. (2013), provided a suitable choice is made for δ (we do not assume a relationship between δ and α because the turbulence in the vortex core is locally generated and unrelated to the disk turbulence, cf. elliptic instability; Lesur & Papaloizou 2010; Lyra & Klahr 2011). The minimum densities occur at the boundary of the vortex, which is the sonic perimeter where shocks occur. Its limit is found by writing the vortex velocity (Equation (8)) as a Mach number:

$$\mathrm{Ma} = \frac{|u_y|}{c_s} = \omega_V \chi \, \frac{x}{H} \qquad (67)$$

and setting $\mathrm{Ma} = 1$. This calculation yields the boundary at

$$a_s = H(\chi \omega_V)^{-1}, \qquad (68)$$

where the subscript s stands for sonic. The Kida solution asymptotically reaches $a_s = 2H/3$, while the GNG solution asymptotically reaches $a_s = H/\sqrt{3}$. In the physical range of relevance ($2 \lesssim \chi \lesssim 10$), both solutions yield values around $H/2$, which matches the results of numerical simulations. Substituting Equation (68) in Equation (36), the gas density contrast is

$$\frac{\rho_{g\,\max}}{\rho_{g\,\min}} = \exp\left[\frac{f^2(\chi)}{2\chi^2 \omega_V^2} \right]. \qquad (69)$$

For neither the Kida nor the GNG solutions does this quantity deviate much from unity. This result is because the argument in the exponent tends asymptotically in both cases to small fractions of f^2; 2/9 in the Kida case, 1/6 in the GNG case.

6.4. Measuring δ

Closed elliptic streamlines are subject to elliptic instability, which leads to subsonic turbulence in the vortex core (Lesur & Papaloizou 2010; Lyra & Klahr 2011). To directly measure δ, the turbulent diffusion parameter, one would need to measure the turbulent velocity field. As α, the Shakura–Sunyaev viscosity parameter (Shakura & Sunyaev 1973), δ can be defined as the ratio of stress over pressure. If the turbulence is isotropic in the midplane, one can write

$$\delta = v_{\mathrm{rms}}^2 / c_s^2, \qquad (70)$$

where v_{rms} is the rms of the turbulent velocities. The beam smearing would render the velocity field unresolved even for moderately close systems, so one should look for unresolved signatures. Spectroscopically, this extra rms velocity should have an effect similar to microturbulence, providing a slight extra broadening in the Doppler core of suitable spectral lines.

For gas temperatures ranging from 20–200 K, assuming that the gas is a 5:2 hydrogen to helium mixture (a mean molecular weight of 2.4), the isothermal sound speeds are in the range 0.26–0.83 km s^{-1}. Considering that typical velocities of subsonic turbulence are $\approx$10% of the sound speed ($\delta \approx 10^{-2}$), the typical velocity signal for 200 K would be of the order of $\leqslant$0.1 km s^{-1}. As van der Marel et al. (2013) quote a sensitivity

limit of 0.2 km s^{-1} for their ALMA observations of Oph IRS 48, only the $\geqslant 2\sigma$ tail of the turbulent velocity field should be detectable.

If a direct determination of δ does not sound promising, an indirect way is possible by measuring S and St. The parameter S can be determined via the dust-density contrast with Equations (66) and (69), or via the dust-gas contrast at maximum (Equation (63)). The Stokes number is

$$\mathrm{St} = \tau_f \Omega = \sqrt{\frac{\pi}{8}} \, \frac{a_\bullet}{H} \, \frac{\rho_\bullet}{\rho_g}, \qquad (71)$$

where $a_\bullet$ is the particle radius and $\rho_\bullet$ is the particle internal density.

6.5. Application to Oph IRS 48

We now apply our model to the observed Oph IRS 48 system, with the parameters derived by van der Marel et al. (2013). The dust contrast in the same orbit is 130, which, according to Equations (67) and (70) for $\chi = 3.1$, sets $S = 4.79$ and $S = 4.82$ for the Kida and the GNG solutions, respectively. The values are close because the gas contrast is small (Equation (69)).

The dust temperature derived by the authors is 60 K. Assuming this temperature is the same as the gas temperature, and a mean molecular weight of 2.4, the isothermal sound speed is $c_s \approx 456$ cm s^{-1}. At $r_0 = 63$ AU, around a 2 $M_\odot$ star, these numbers translate into an aspect ratio of $H/r \approx 0.09$ or $H \approx 5.4$ AU. As for the particle radius, the ALMA data are sensitive up to $a_\bullet \approx 1.5$ mm, and we take this size to be representative.

The gas mass is quoted to range between 19 and 27 Jupiter masses, measured from a ring centered at 60 AU. The signal-to-noise is too low to derive a radial extent, but assuming it ranges between 50–70 AU, the gas surface density should range between 20–30 g cm^{-2}. We take $\Sigma_g = 25$ g cm^{-2} as the best estimate, which, for the scale height derived above, translates into $\rho_g = \Sigma_g/(\sqrt{2\pi} H) \approx 1.25 \times 10^{-13}$ g cm^{-3}.

For particles of material density $\rho_\bullet = 0.8$ g cm^{-3}, the Stokes number should then be St ≈ 0.008. For $S = 4.8$, these numbers translate into $\delta \approx 1.5 \times 10^{-3}$, meaning that typical turbulent velocities in the vortex core are $\sqrt{\delta} \approx 4\%$ of the sound speed. These velocities fall squarely within the range expected for the elliptic instability (Lesur & Papaloizou 2010; Lyra & Klahr 2011), which shows a maximum speed of 10% of the speed of sound.

As for the trapped mass, van der Marel et al. (2013) measure 9 $M_\oplus$. For the typical interstellar dust-to-gas ratio of $\varepsilon = 0.01$, Equation (65) yields 6 and 17 $M_\oplus$ for the Kida and GNG solutions, respectively. Given the approximations, assumptions, and uncertainties, an agreement within a factor of two is remarkable.

Although these values seem reasonable, it should be noted that for Oph IRS 48 the candidate planet is at $\approx$20 AU, whereas the dust trap is at 63 AU. Even though the planet is supposed to be massive (planet-to-star mass ratio 5×10^{-3}), gaps are not expected to be that wide. The supposed vortex also seems to be very big, with a semiminor axis of 17 AU. For a temperature of 60 K, this value corresponds to over 3H, which is far from the $\approx H/2$ expected from numerical simulations and Equation (68). Relaxing the approximation that the gas and dust have the same temperature does little to solve the discrepancy. Because $H \propto c_s \propto \sqrt{T}$, a vortex six times bigger means a temperature thirty-six times hotter. These numbers would bring the gas temperature above 2000 K, which is unrealistic.

7. CONCLUSIONS

We solve for the distribution of dust trapped in disk vortices, in the steady state between the gas drag, which tends to drive dust into the vortex, and diffusion, which expels it. Equations (31) and (34), with a coefficient given by Equation (63), are our result for a distribution with "axis-symmetry" in the coordinate system defined by Equations (18) and (19). That is, the coordinate system consists of ellipses of equal aspect ratios as those of the gas vortex. The solution has some remarkable properties. It is a Gaussian with a standard deviation H_V, where, given the angular velocity Ω_V of the vortex, H_V is determined by three quantities: the sonic length and gas scale height, H; the vortex aspect ratio χ; and $S = \mathrm{St}/\delta$, the relative strength of drag to diffusion. The importance of this last parameter had already been hinted by Cuzzi et al. (1993) and Dubrulle et al. (1995) in the context of steady states of dust sedimentation, and by Klahr & Henning (1997) for vortices in the meridional plane. An insightful study by Jacquet et al. (2012) emphasized the relevance of this parameter for the global redistribution of solids. Birnstiel et al. (2013) also find S to be the parameter of relevance in their semi-analytical model.

Transitional disks provide an interesting venue in which to test the model in an astrophysical context, since all three parameters are derivable from the data. The vortex aspect ratio is readily observable and H follows from the temperature ($H = c_s/\Omega$). The parameter S follows from the density contrast (either the dust-gas contrast at maximum or the dust contrast in the same orbit). Disentangling St from δ in this parameter requires the direct measurement of at least one of these quantities. The diffusion parameter δ is in principle not equal to α (the dimensionless gas viscosity of Shakura & Sunyaev 1973) because the processes generating turbulence in the vortex and in the disk are different. The latter is supposedly the MRI, whereas the former is the elliptic or magneto-elliptic instability (see Lyra 2013 and references therein). A direct measure of δ would require measuring the velocity field inside the vortex that would appear spectroscopically as a slight extra line broadening. However, this technique would be difficult because the signal is too small. Measuring St requires knowing the gas density and temperature, the particle radius, and the internal density. Of these, the internal density is difficult to measure directly and should be inferred from laboratory experiments. We apply the model to the Oph IRS 48 system, finding consistent values. The Stokes number for the 1.5 mm particles is estimated to be St $\approx$ 0.008, implying $\delta \approx 1.5 \times 10^{-3}$, and turbulent velocities are in agreement with numerical simulations. The total dust masses we estimate are within a factor two of the measured value.

We also solve for the non-axisymmetric problem, showing that, for the vortex core, it is in general only a small correction. The solution is Equation (38), with "radial" basis functions given by Equation (50) and coefficients given by Equation (52). In practice, the magnitude of the higher non-axisymmetric modes decreases quickly as m increases, and only the $m = 2$ term would provide an appreciable deviation from ν-symmetry. We find that non-axisymmetry in dust is associated with non-zero pressure gradients along elliptical streamlines of the vortex.

We recall that aside from planetary gap edges, self-sustained disk vortices may also result from either the RWI at the boundary between the MRI-active and dead zones, or convective-like nonlinear baroclinic instabilities (Klahr & Bodenheimer 2003; Klahr 2004; Petersen et al. 2007a, 2007b; Lesur & Papaloizou 2010; Lyra & Klahr 2011; Raettig et al. 2013). These processes, however, are not reasonable in the context of the outer regions of transition disks: the outer edge of the dead zone is quite smooth (Dzyurkevich et al. 2013; Landry et al. 2013), whereas the RWI requires a sharp enough transition; as for the baroclinic instability, it requires finite thermal diffusion, whereas the thin outer disk is supposed to radiate efficiently. These arguments leave the gap-edge RWI as the only currently known plausible mechanism to excite such vortices. However, this interpretation is not without difficulties, because, as noted in Section 6.5, the dust trap is too far out (63 AU) to be the result of a gas gap carved by a planet at 20 AU, and because its radial size ($\approx$35 AU) would imply an unrealistically high gas temperature. Future modeling should be directed at solving these discrepancies.

REFERENCES

Adams, F. C., & Watkins, R. 1995, ApJ, 451, 314
Alexander, R. D., Clarke, C. J., & Pringle, J. E. 2006, MNRAS, 369, 216
Andrews, S. M., Wilner, D. J., Espaillat, C., et al. 2011, ApJ, 732, 42
Ataiee, S., Pinilla, P., Zsom, A., et al. 2013, A&A, 553, 3
Balbus, S. A., & Hawley, J. F. 1991, ApJ, 376, 214
Barge, P., & Sommeria, J. 1995, A&A, 295, L1
Birnstiel, T., Andrews, S. M., & Ercolano, B. 2012, A&A, 544, 79
Birnstiel, T., Dullemond, C. P., & Pinilla, P. 2013, A&A, 550, L8
Brauer, F., Dullemond, C. P., Johansen, A., et al. 2007, A&A, 469, 1169
Brown, J. M., Blake, G. A., Qi, C., et al. 2009, ApJ, 704, 496
Bryden, G., Chen, X., Lin, D. N. C., Nelson, R. P., & Papaloizou, J. C. B. 1999, ApJ, 514, 344
Calvet, N., D'Alessio, P., Hartmann, L., et al. 2002, ApJ, 568, 1008
Calvet, N., D'Alessio, P., Watson, D. M., et al. 2005, ApJ, 630, 185
Calvet, N., Muzerolle, J., Briceño, C., et al. 2004, AJ, 128, 1294
Casassus, S., Perez, M. S., Jordán, A., et al. 2012, ApJ, 754, 31
Casassus, S., van der Plas, G., Perez, S., et al. 2013, Natur, 493, 191
Chang, P., & Oishi, J. S. 2010, ApJ, 721, 1593
Charnoz, S., Fouchet, L., Aleon, J., & Moreira, M. 2011, ApJ, 737, 33
Chavanis, P. H. 2000, A&A, 356, 1089
Cieza, L. A., Schreiber, M. R., Romero, G. A., et al. 2010, ApJ, 712, 925
Cieza, L. A., Swift, J. J., Mathews, G. S., & Williams, J. P. 2008, ApJ, 686, 115
Clarke, C. J., & Owen, J. E. 2013, MNRAS, 433, L69
Clarke, C. J., & Pringle, J. E. 1988, MNRAS, 235, 365
Corder, S., Eisner, J., & Sargent, A. 2005, ApJ, 622, 133
Currie, Th. 2010, arXiv:1002.1715
Currie, Th., Lada, C. J., Plavchan, P., et al. 2009, ApJ, 698, 1
Currie, Th., & Sicilia-Aguilar, A. 2011, ApJ, 732, 24
Cuzzi, J. N., Dobrovolskis, A. R., & Champney, J. M. 1993, Icar, 106, 102
de Val-Borro, M., Artymowicz, P., D'Angelo, G., & Peplinski, A. 2007, A&A, 471, 1043
de Val-Borro, M., Edgar, R. G., Artymowicz, P., et al. 2006, MNRAS, 370, 529
Dominik, C., & Dullemond, C. P. 2008, A&A, 491, 663
Dubrulle, B., Morfill, G., & Sterzik, M. 1995, Icar, 114, 237
Dzyurkevich, N., Turner, N. J., Henning, Th., & Kley, W. 2013, ApJ, 765, 114
Espaillat, C., Calvet, N., Luhman, K. L., Muzerolle, J., & D'Alessio, P. 2008, ApJL, 682, L125
Gauvin, L. S., & Strom, K. M. 1992, ApJ, 385, 217
Godon, P., & Livio, M. 1999, ApJ, 523, 350
Godon, P., & Livio, M. 2000, ApJ, 537, 396
Goldreich, P., & Ward, W. R. 1973, ApJ, 183, 1051
Goodman, J., Narayan, R., & Goldreich, P. 1987, MNRAS, 225, 695

Hawley, J. F. 1987, MNRAS, 225, 677
Inaba, S., & Barge, P. 2006, ApJ, 649, 415
Ireland, M. J., & Kraus, A. L. 2008, ApJL, 678, L59
Isella, A., Pérez, L. M., & Carpenter, J. M. 2012, ApJ, 747, 136
Isella, A., Pérez, L. M., Carpenter, J. M., et al. 2013, ApJ, submitted
Jacquet, E., Gounelle, M., & Fromang, S. 2012, Icar, 220, 162
Johansen, A., Andersen, A. C., & Brandenburg, A. 2004, A&A, 417, 361
Johansen, A., Oishi, J. S., Mac Low, M.-M., et al. 2007, Natur, 448, 1022
Kida, S. 1981, JPSJ, 50, 3517
Klahr, H. 2004, ApJ, 606, 1070
Klahr, H., & Bodenheimer, P. 2003, ApJ, 582, 869
Klahr, H. H., & Henning, Th. 1997, Icar, 128, 213
Klahr, H., & Kley, W. 2006, A&A, 445, 747
Kley, W., Müller, T. W. A., Kolb, S. M., Benítez-Llambay, P., & Masset, F. 2012, A&A, 546, 99
Kley, W., & Nelson, R. P. 2012, ARA&A, 50, 211
Landry, R., Dodson-Robinson, S. E., Turner, N. J., & Abram, G. 2013, ApJ, 771, 80
Lesur, G., & Papaloizou, J. C. B. 2010, A&A, 513, 60
Lin, D. N. C., & Papaloizou, J. 1986a, ApJ, 307, 395
Lin, D. N. C., & Papaloizou, J. 1986b, ApJ, 309, 846
Lin, M.-K. 2012a, ApJ, 754, 21
Lin, M.-K. 2012b, MNRAS, 426, 3211
Lin, M.-K. 2013, ApJ, 765, 84
Lin, M.-K., & Papaloizou, J. C. B. 2011a, MNRAS, 415, 1426
Lin, M.-K., & Papaloizou, J. C. B. 2011b, MNRAS, 415, 1445
Lin, M.-K., & Papaloizou, J. C. B. 2012, MNRAS, 421, 780
Lovelace, R. V. E., & Hohlfeld, R. G. 1978, ApJ, 221, 51
Lovelace, R. V. E., Li, H., Colgate, S. A., & Nelson, A. F. 1999, ApJ, 513, 805
Lyra, W. 2013, in Instabilities and Structures in Proto-Planetary Disks, ed. P. Barge & L. Jorda, EPJ Web of Conferences, Volume 46, 04003
Lyra, W., & Klahr, H. 2011, A&A, 527A, 138
Lyra, W., Johansen, A., Klahr, H., & Piskunov, N. 2009a, A&A, 493, 1125
Lyra, W., Johansen, A., Klahr, H., & Piskunov, N. 2008, A&A, 491, L41
Lyra, W., Johansen, A., Zsom, A., Klahr, H., & Piskunov, N. 2009b, A&A, 497, 869
Lyra, W., & Mac Low, M.-M. 2012, ApJ, 756, 62
Lyttleton, R. A. 1972, MNRAS, 160, 255
Masset, F., & Snellgrove, M. 2001, MNRAS, 320, L55
Méheut, H., Casse, F., Varnière, P., & Tagger, M. 2010, A&A, 516, 31
Méheut, H., Cong, Y., & Lai, D. 2012a, MNRAS, 422, 2399
Méheut, H., Keppens, R., Casse, F., & Benz, W. 2012b, A&A, 542A, 9
Méheut, H., Meliani, Z., Varnière, P., & Benz, W. 2012c, A&A, 545, 134
Merín, B., Brown, J. M., Oliveira, I., et al. 2010, ApJ, 718, 1200
Morfill, G. E., & Voelk, H. J. 1984, ApJ, 287, 371
Muto, T., Grady, C. A., Hashimoto, J., et al. 2012, ApJL, 748, L22
Muzerolle, J., Adame, L., D'Alessio, P., et al. 2006, ApJ, 643, 1003
Muzerolle, J., Allen, L. E., Megeath, Th., Hernández, J., & Gutermuth, R. A. 2010, ApJ, 708, 1107

Najita, J. R., Strom, S. E., & Muzerolle, J. 2007, MNRAS, 378, 369
Nelson, R. P., Papaloizou, J. C. B., Masset, F., & Kley, W. 2000, MNRAS, 318, 18
Oppenheimer, B. R., Brenner, D., Hinkley, S., et al. 2008, ApJ, 679, 1574
Owen, J. E., Ercolano, B., Clarke, C. J., & Alexander, R. D. 2010, MNRAS, 401, 1415
Paardekooper, S.-J., & Mellema, G. 2004, A&A, 425, L9
Papaloizou, J., & Lin, D. N. C. 1984, ApJ, 285, 818
Papaloizou, J. C. B., & Pringle, J. E. 1984, MNRAS, 208, 721
Papaloizou, J. C. B., & Pringle, J. E. 1985, MNRAS, 213, 799
Pascucci, I., & Sterzik, M. 2009, ApJ, 702, 724
Petersen, M. R., Julien, K., & Stewart, G. R. 2007a, ApJ, 658, 1236
Petersen, M. R., Stewart, G. R., & Julien, K. 2007b, ApJ, 658, 1252
Piétu, V., Guilloteau, S., & Dutrey, A. 2005, A&A, 443, 945
Pinilla, P., Benisty, M., & Birnstiel, T. 2012b, A&A, 545, 81
Pinilla, P., Birnstiel, T., Ricci, L., et al. 2012a, A&A, 538, 114
Quillen, A. C., Blackman, E. G., Frank, A., & Varnière, P. 2004, ApJ, 612, 137
Raettig, N., Lyra, W., & Klahr, H. 2013, ApJ, 765, 115
Regály, Zs., Juhász, A., Sándor, Zs, & Dullemond, C. P. 2012, MNRAS, 419, 1701
Regev, O., & Umurhan, O. M. 2008, A&A, 468, 341
Rosotti, G. P., Ercolano, B., Owen, J. E., & Armitage, P. J. 2013, MNRAS, 430, 1392
Safronov, V. S. 1969, Evoliutsiia Doplanetnogo Oblaka (English transl: 1972, Evolution of the Protoplanetary Cloud and Formation of Earth and the Planets, NASA Tech. Trans. F-677; Jerusalem: Israel Sci. Transl.)
Sicilia-Aguilar, A., Hartmann, L. W., Fürész, G., et al. 2006, AJ, 132, 2135
Shakura, N. I., & Sunyaev, R. A. 1973, A&A, 24, 337
Skrutskie, M. F., Dutkevitch, D., Strom, S. E., et al. 1990, AJ, 99, 1187
Strom, K. M., Strom, S. E., Edwards, S., Cabrit, S., & Skrutskie, M. F. 1989, AJ, 97, 1451
Tagger, M. 2001, A&A, 380, 750
Tang, Y.-W., Guilloteau, S., Piétu, V., et al. 2012, A&A, 547, 84
Tanga, P., Babiano, A., Dubrulle, B., & Provenzale, A. 1996, Icar, 121, 158
Toomre, A. 1981, in The Structure and Evolution of Normal Galaxies (Cambridge: Cambridge Univ. Press), 111
van der Marel, N., van Dishoeck, E. F., Bruderer, S., et al. 2013, Sci, 340, 1199
Varnière, P., & Tagger, M. 2006, A&A, 446, 13
Wolk, S. J., & Walter, F. M. 1996, AJ, 111, 2066
Youdin, A. 2008, arXiv:0807.1114
Youdin, A. N., & Goodman, J. 2005, ApJ, 620, 459
Youdin, A. N., & Shu, F. H. 2002, ApJ, 580, 494
Zhang, H., & Lai, D. 2006, MNRAS, 368, 917
Zhu, Zh., Nelson, R. P., Hartmann, L., Espaillat, C., & Calvet, N. 2011, ApJ, 729, 47
Zsom, A., Ormel, C. W., Dullemond, C. P., & Henning, Th. 2011, A&A, 534, 73